The Doppler effect on indirect detection of dark matter

Devon Powell,[1, 2, *] Ranjan Laha,[1, 2, †] and Tom Abel[1, 2]

[1]*Kavli Institute for Particle Astrophysics and Cosmology (KIPAC),*
Department of Physics, Stanford University, Stanford, CA 94305, USA
[2]*SLAC National Accelerator Laboratory, Menlo Park, CA 94025, USA*

(Dated: October 17, 2016)

[1]

I Introduction: The search for the particle properties of dark matter is one of the most important research avenues [2–4]. The "weak" interactions experienced by the dark matter particle complicates these searches. Despite decades of multi-pronged searches, we have not yet identified the dark matter particle [5]. One of the most important ways to search for dark matter particles is indirect detection [6].

Many anomalous signals have been interpreted as arising from dark matter interactions [7–15]. Astrophysical sources such as pulsars or atomic lines are diverse enough to mimic a dark matter signal [16–21]. The separation of signal and background is difficult since one needs to model these in the same data set. Taking lessons from all these misadventures, it is prudent to ask for new methods to cleanly separate the signal and background. This is especially important since there are many viable dark matter candidates which can only be detected via astrophysical observations.

Distinct kinematic signatures arising from dark matter annihilation or decay are used to separate the dark matter signal from background. These signatures include monochromatic photons arising from dark matter annihilation or decay. Past experiences have shown that it is not reliable to only depend on this kinematic end point signature for the identification of a dark matter signal. Additional checks are required to completely confirm a dark matter signal.

In order to better characterize a dark matter signal, Ref. [1] utilized the superb energy resolution, $\sim \mathcal{O}(0.1\%)$, of Hitomi (previously known as Astro-H) to find a new signature — dark matter velocity spectroscopy. Solar motion around the Galaxy produces a distinct longitudinal dependence in the dark matter signal, a signature of Doppler effect. This new signature is model independent and applicable to any dark matter signal containing a sharp feature. It is unlikely that baryonic phenomenon can produce such a distinct signature [1].

Given the importance of dark matter particle searches, it is important to characterize any new model independent signature in detail. While Hitomi had a narrow field of view, it is important to confirm if dark matter velocity spectroscopy can also be performed by a high energy

resolution instrument with a wide field of view. We perform such a study in this work using dark matter only simulations from Ref. [22]. As an example of the dark matter signal, we consider the 3.5 keV line [13, 14]. The status of the 3.5 keV line is controversial [23–32]. The malfunctioning of the Hitomi satellite did not permit an observation to conclusively test this signal. We use future Micro-X observations [33] to demonstrate our technique. It is expected that Micro-X will have an energy resolution of 3 eV at 3.5 keV [33], a high enough energy resolution to permit dark matter velocity spectroscopy [1]. We emphasize that we are using this 3.5 keV signal as a proxy, and that the underlying physics of dark matter velocity spectroscopy is model independent.

There have been many works in which velocity spectroscopy was used to understand baryonic astrophysical emission [34–37]. Ref. [1] first applied this technique analytically to dark matter. In this work, we analyze for the *first* time dark matter velocity spectroscopy using realistic dark matter simulations

Any telescope with $\mathcal{O}(0.1\%)$ energy resolution can perform dark matter velocity spectroscopy. An improvement in the energy resolution is the natural step in the evolution of telescope instrumentation. This improvement will help in disentangling the dark matter signal from background, and improve our knowledge of the astronomical sources. For certain wavelengths, it is already known how to build a detector with $\mathcal{O}(0.1\%)$ energy resolution, such as INTEGRAL/ SPI [38] and Hitomi. Near future instruments like Micro-X [33] and ATHENA X-IFU [39] will also have $\mathcal{O}(0.1\%)$ energy resolution.

II Theory: In this section, we outline the theoretical insights leading to dark matter velocity spectroscopy [1]. The discussion is tailored for a wide field of view instrument like Micro-X. In this work, we are concerned with sterile neutrino, ν_s, decay to an active neutrino, ν_a, and a photon, γ: $\nu_s \rightarrow \nu_a + \gamma$. This implies that the photon energy $E = m_s/2$. We concentrate on the detection of photons in this work, as the constraint from the detection of active neutrino is weak.

A Derivation: We now derive the main analytic expressions needed for velocity spectroscopy. For notational convenience, we define the postiion vector $\mathbf{r} = \mathbf{r}(s, \Omega)$, where s is the distance along the line of

---

[*]dmpowel1@stanford.edu
[†]rlaha@stanford.edu

sight Ω.

For instruments with an energy resolution $\Delta E/E \gg \mathcal{O}(0.1\%)$, the differential flux of photons originating from dark matter decay in the Milky Way halo is given by [33]:

$$\frac{d^2\mathcal{F}}{d\Omega\,dE} = \frac{\Gamma}{4\pi\,m_s}\frac{dN}{dE}\int_0^{s_{\max}} ds\,\rho(\mathbf{r}). \quad (1)$$

Here $\mathcal{F}$ denotes the flux in $\mathrm{cm}^{-2}\,\mathrm{s}^{-1}$, Ω denotes the solid angle in sr, E denotes the energy of the photon in keV, and Γ denotes the decay rate (in s^{-1}) of the dark matter particle of mass m_s (in keV). The dark matter density (in keV cm^{-3}) profile is denoted by $\rho(\mathbf{r})$, and the photon spectrum (in keV^{-1}) is denoted by $dN(E)/dE$. The line of sight distance s, varies from 0 to $s_{\max}$, where the maximum value of the line of sight distance $s_{\max}$ corresponds to the virial radius of the Milky Way halo.

Observation by a telescope with $\sim \mathcal{O}(0.1\%)$ energy resolution modifies this above expression, Eqn. 1, in two important and distinct ways. First, the photon line is broadened due to the velocity dispersion of the dark matter particles in the Milky Way halo. Second, the energy of the photon is shifted depending on the Doppler shifting of the line.

We take into account the broadening of the line by convolving $dN(E)/dE$ by a Gaussian of width $\sigma_E = (E/c)\sigma_{v_{\mathrm{LOS}}}$ [1]. Here $\sigma_{v_{\mathrm{LOS}}}(\mathbf{r})$ is the line of sight velocity dispersion of dark matter. The Gaussian form arises since we consider a Maxwellian dark matter velocity distribution. The line shape will change if we consider dark matter velocity distribution favored by recent hydrodynamical simulations [40–42], but we ignore the difference in this work.

The broadened line spectrum can be written as

$$\frac{d\tilde{N}(E,\mathbf{r})}{dE} = \int dE' \frac{dN(E)}{dE} G(E - E', \sigma_{E'}(\mathbf{r})), \quad (2)$$

where the convolution function is a Gaussian as mentioned above. The width of the Gaussian, $\sigma_E(\mathbf{r})$ is calculated following Ref. [1].

Since the solar velocity is nonrelativistic, we can use the usual formula for Doppler shift: $\delta E/E = -v_{\mathrm{LOS}}/c$. Following Ref. [1], we define $v_{\mathrm{LOS}} = (\langle \mathbf{v}_\chi \rangle - \mathbf{v}_\odot) \cdot \hat{r}_{\mathrm{LOS}}$. We assume $\langle \mathbf{v}_\chi \rangle \approx 0$, and $v_\odot = 220\,\mathrm{km\,s}^{-1}$. In the coordinate system where the x-axis is towards the Galactic Center, the direction of the Galactic rotation is in the y direction, and the z-axis is the normal to the Galactic plane, we have $\mathbf{v}_\odot = v_\odot \hat{y}$. In this reference frame, $\mathbf{v}_\odot \cdot \hat{r}_{\mathrm{LOS}} = v_\odot y/|r_{\mathrm{LOS}}|$. In terms of the Galactic longitude, ℓ, and Galactic latitude, b, we have $y = r_{\mathrm{LOS}}\sin\ell\cos b$. From this, we have $v_{\mathrm{LOS}} = v_\odot \sin\ell\cos b$.

Taking these two effects into account, we can rewrite Eqn. 1 as

$$\begin{aligned}\frac{d^2\mathcal{F}}{d\Omega\,dE} &= \frac{\Gamma}{4\pi\,m_s}\int_0^{s_{\max}} ds\,\rho(\mathbf{r}) \\ &\times \frac{d\tilde{N}[E(1 - v_{\mathrm{LOS}}(\mathbf{r})/c), \mathbf{r}]}{dE}.\end{aligned} \quad (3)$$
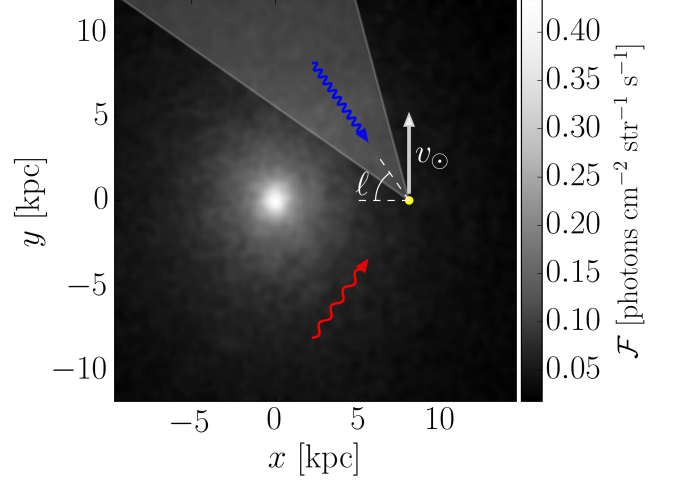

FIG. 1: The projected column density of Halo 374, the most spherical halo in the suite of simulations used here. The color scale is given in units of the surface brighness observed at the distance of the Sun, 8 kpc from the halo center. The diagram illustrates the basic principle of velocity spectroscopy: X-ray photons due to sterile netrino decay are collected from within the field of view (shaded triangle) at the Sun's position. The net blue- or redshift of observed photons is determined by the line of sight relative to the Sun's velocity. In this simple model, the energy shift $\delta E/E = (v_\odot/c)\sin\ell$.

An important difference in the narrow field of view and wide field of view instruments is encapsulated in the term $E(1 - v_{\mathrm{LOS}}(\mathbf{r})/c)$. For Hitomi with a field of view of 9 arcmin^2, the maximum value of the line intensity approximately occurs at the center of the field of view. This is not true for a wide field of view instrument like Micro-X (20° radius field of view). The maximum value of the line intensity depends on the density profile as is evident from Eqn. 3.

The shift in the central value of the energy of the widened line is shown by the argument $(E/c)v_{\mathrm{LOS}}(\mathbf{r})/c$. Both the width and observed energy of the line are determined by the position $\mathbf{r}$ of the emission, indicated by $\mathbf{r}$ in the argument of $d\tilde{N}/dE$.

B   Analytic model: Here we describe the analytic model to which we compare the results of our N-body analysis. For our purposes, we assume that dN/dE is a line. Thus, $d\tilde{N}/dE$ is a Gaussian of width σ_E in accordance with Eqn. (2).

We begin with the total flux, which is found simply by integrating the J-factor over the field of view.

$$\mathcal{F} = \frac{\Gamma}{4\pi\,m_s}\int_\Omega\int_0^{s_{\max}} d\Omega\,ds\,\rho(\mathbf{r}) \quad (4)$$

Note that in the limit of a small FOV, the J-factor can be assumed constant over the FOV. As we consider a

large FOV instrument here, we retain the full form of this integral in our calculations.

The observed Doppler shift is given in terms of the LOS velocity, weighted by the flux:

$$\langle v_{\rm LOS} \rangle = \frac{1}{\mathcal{F}} \frac{\Gamma}{4\pi\, m_s} \int_\Omega \int_0^{s_{\rm max}} d\Omega\, ds\, \rho(\mathbf{r})\, v_{\rm LOS}(\mathbf{r}) \quad (5)$$

Again, in the limit of a small FOV, it is easy to see that in terms of Galactic longitude and latitude (ℓ, b), $\langle v_{\rm LOS} \rangle = v_\odot \sin \ell \cos b$. We refer to this hereafter as the "simple sinusoid model".

Finally, the Doppler-broadened width of the line can be expressed simply when $d\tilde{N}/dE$ is a Gaussian:

$$\langle \sigma^2_{v_{\rm LOS}} \rangle = \frac{1}{\mathcal{F}} \frac{\Gamma}{4\pi\, m_s} \int_\Omega \int_0^{s_{\rm max}} d\Omega\, ds\, \rho(\mathbf{r})$$
$$\times [(v_{\rm LOS}(\mathbf{r}) - \langle v_{\rm LOS} \rangle)^2 + \sigma^2_{v_{\rm LOS}}(\mathbf{r})] \qquad (6)$$

We compute these integrals analytically using a standard numerical quadrature routine.

III   Methods:

A   Simulations: Numerical simulations take into account many different processes which participate in dark matter halo formation. Many signatures of these non linear processes are not taken into account in an analytical model of the dark matter halo. It is thus important to validate any new signature of dark matter by using realistic simulations of galaxy formation.

We evaluate the potential of dark matter velocity spectroscopy using dark-matter-only N-body simulations. We study a suite of Milky Way analogues run using the L-GADGET cosmology code (a descendant of GADGET-2 [43]). These are dark-matter-only zoom-in simulations run by Ref. [22] to study subhalo abundance. Their high resolution and multiple realizations makes them suitable for our purposes as well. Each halo has $\mathcal{O}(10^7)$ high-resolution particles with a particle mass $m_p = 4.0 \times 10^5 M_\odot$ and total mass $M_{\rm vir} \simeq 10^{12} M_\odot$ (masses in physical units). Refer to [22] for the full description of the simulation parameters.

We note that a 7 keV sterile neutrino has a non-negligible free-streaming length and hence introduces a cutoff in the matter power spectrum at a wavenumer $k_{\rm WDM} \simeq 10$ Mpc^{-1} h [44]. This gives a corresponding mass scale cutoff of $M_{\rm WDM} \simeq 10^{10}$ M$_\odot$, or roughly 10^{-2} of the Milky Way halo mass. As we are interested in the main halo itself, we do not concern ourself with the slight differences on smaller mass scales that may arise due to our use of pure CDM simulations as a proxy for sterile neutrino dark matter. Ref. [45] discusses this in further detail and note that the flux maps for cold versus keV-mass dark matter haloes differ by a few percent at most. While we focus on $m_s = 7$ keV here, one should view this study as a test model while noting that the velocity spectroscopy approach is valid over a wide range of particle masses.

Among the 46 halo realizations, we focus on one halo, Halo 374, (Figure 1) in detail. This is the most spherically-symmetric halo, with principal axis ratios $b/a = 0.86$ and $c/a = 0.73$. We choose this halo to facilitate the comparison of our results with a spherically symmetric generalized NFW profile of the halo. Dark-matter-only simulations produce triaxial halos, but recent hydrodynamical simulations have shown that the inclusion of baryons tend to sphericalize a halo [46–49].

Although hydrodynamical models are investigated by many groups, yet it is not known if all the baryonic processes are self consistently taken into account in these simulations. To take into account these uncertainties, we will also show our results for halos which are less spherical compared to Halo 374. The statistical significance of the result depends on the triaxiality of the halo.

B   Velocity spectroscopy using simulations: In order to generalize the analytical methods presented in Sec. II to a simulation containing N-body particles, we simply convert the integration to a sum over the N-body particles. This is similar in spirit to the "sightline" method employed by [45] and the velocity distribution function sampling of [50]. We construct the full spectral intensity seen by the detector directly from the N-body particles, incorporating Doppler shift and velocity dispersion in a natural way.

The total flux can be found by integrating the differential flux in Eqn. 1 over the energy and solid angle. Implementing this in an N-body simulation implies a summation over all of the particles, p, within the field of view, Ω, and weighting by the inverse square of the scalar distance to the observer, r_p^{-2}:

$$\mathcal{F} = \frac{\Gamma}{4\pi\, m_s} \sum_{p \in \Omega} \frac{m_p}{r_p^2}, \qquad (7)$$

The differential flux in energy can also be calculated in a similar way:

$$\frac{d\mathcal{F}}{dE} = \frac{\Gamma}{4\pi\, m_s} \sum_{p \in \Omega} \frac{m_p}{r_p^2} \frac{dN[E(1 - v_p/c)]}{dE}, \qquad (8)$$

where v_p is the velocity of particle p projected along the line of sight to the observer. By considering the LOS velocity of each particle independently, we automatically capture the spectral convolution introduced by the bulk velocity dispersion.

We focus here on the special case where dN/dE is a line due to sterile neutrino decay. The parameters of the sterile neutrino are those favored by the 3.5 keV line [13]. In this case, computing the observed spectrum is then as simple as building a flux-weighted histogram of the line-of-sight velocities for all particles in the sampling cone. In practice we find $d\mathcal{F}/dE$ to be very nearly Gaussian. We compare the line width and shift computed analytically and directly from simulations in Fig. 2 for six different fields of view at $b = 25°$. The analytical computation

is shown by dashed line, whereas the solid line shows the lines computed directly from the simulations. Good agreement is seen between these two different computations for this halo.
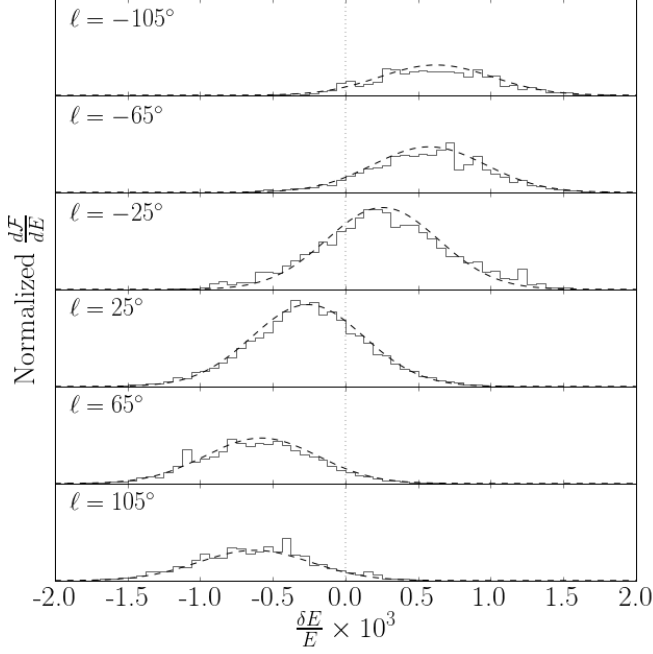

FIG. 2: We plot the decay line spectrum $d\mathcal{F}/dE$ as a function of fractional shift in the energy $\delta E/E$ for six different pointings ℓ, with $b = 25°$. This compares the empirical histograms (solid) computed from the N-body simulation against the analytic Gaussian model (dashed) computed from an NFW profile with an analytic velocity dispersion model. The Gaussian line profile agrees closely with the empirical spectrum. The data for all six pointings are normalized relative to one another, and the x-axis is multiplied by 1000 for clarity.

C Synthetic observation by Micro-X: The instrument that we focus on in this work is Micro-X[33]. It is a direct successor to the XQC sounding rocket experiment[51–53]. We follow the parameters of the instrument near 3.5 keV as mentioned in [33]: 20° radius field of view, effective area 1 cm^2 , 96% detector efficiency, 300 s exposure time, and 3 eV energy resolution (FWHM). For convenience we combine these instrumental parameters into the exposure factor $O_{MX} = 288$ cm^2 s.

To minimize contamination by the Galactic plane, we focus on fields of view which are centered at $b = 25°$ for various different Galactic longitudes, ℓ. This choice is a compromise between the decreasing signal strength away from the Galactic Center, and the more rapidly decreasing background away from the Galactic plane. A typical sterile neutrino decay flux at 3.5 keV from the Milky Way halo at $b = 25°$ is $\mathcal{F} \sim 0.1$ photons cm^{-2} str^{-1} s^{-1} for a signal count $N_s \sim 3 - 12$ photons, depending on ℓ.

We model the background N_b using the cosmic X-ray background model of [54]. The use of an alternative model[55] for the cosmic X-ray background does not alter our conclusions. For our analysis, we consider all photons observed in the range 3.5 keV $\pm$ 10.5 eV. This range contains all of the expected signal and captures sufficient background counts for signal and background to be differentiated effectively. The background spectrum is constant to within 1% over this small range, so we fit a flat spectrum in our analysis. A typical background count in this energy window is $N_b \sim 3$ photons per pointing.

Our synthetic observation itself consists of a Monte Carlo sampling of photons from the N-body particles and the background model. For each particle $p \in \Omega$ in the sampling cone, we sample $n_p \sim \text{Poisson}(\lambda_p)$ photons, where the expected photon count per particle $\lambda_p = \frac{\Gamma O_{\text{MX}} m_p}{4\pi m_s r_p^2}$. Each signal photon is given energy $E_i \sim \mathcal{N}[E(1 - v_p/c), \sigma_{\text{instr}}]$ to model the energy resolution of the instrument. In addition, we sample $n_b \sim \text{Poisson}(\lambda_b)$ background photons, where the rate λ_b is determined by the background model [54], and endow each with energy $E_i \sim \text{Uniform}(3.5 \text{ keV} \pm 10.5 \text{ eV})$.

We then attempt to reconstruct the sterile neutrino decay line from the synthetic photons $\{E_i\}$. A major challenge in this work is differentiating between small numbers of signal vs. background photons in order to determine the line energy. To this end, we use an extended maximum likelihood analysis for each pointing ℓ. This is an unbinned analysis described by [56] which allows us to estimate the signal parameters E and σ_E as well as the signal and background counts N_s and N_b simultaneously. [33] uses this analysis as well, as it gives good fits to unbinned data for small number counts.

Our likelihood function is

$$\mathcal{L}(E, \sigma_E, N_s, N_b; \{E_i\}) =$$
$$\frac{e^{-(N_s+N_b)}}{N!} \prod_{i=1}^{N} \left(\frac{N_s e^{\frac{-(E_i-E)^2}{2(\sigma_E^2 + \sigma_{\text{instr}}^2)}}}{\sqrt{2\pi(\sigma_E^2 + \sigma_{\text{instr}}^2)}} + \frac{N_b}{\sigma_b} \right) \quad (9)$$

Fixed parameters are the total number of observed photons N, the energy range over which the likelihood is fit $\sigma_b = 21$ eV, and the Gaussian equivalent instrumental energy resolution $\sigma_{\text{instr}} = 1.3$ eV. The use of σ_{instr} in our fit models the uncertainty in the observed photon energies E_i and serves to regularize the problem. We give an example of one such synthetic observation and extended likelihood fit in Figure 3.

Our figure of merit for a detection of a Doppler-shifted line is the probability that the data exclude zero shifting. In other words, we consider the energy shift of the line centroid away from $\delta E/E = 0$ in units of σ_{cent}, the uncertainty in the line energy.

[56] gives a prescription for obtaining the covariance matrix between the four fitted parameters, which we use to compute σ_{cent}. This naturally incorporates the
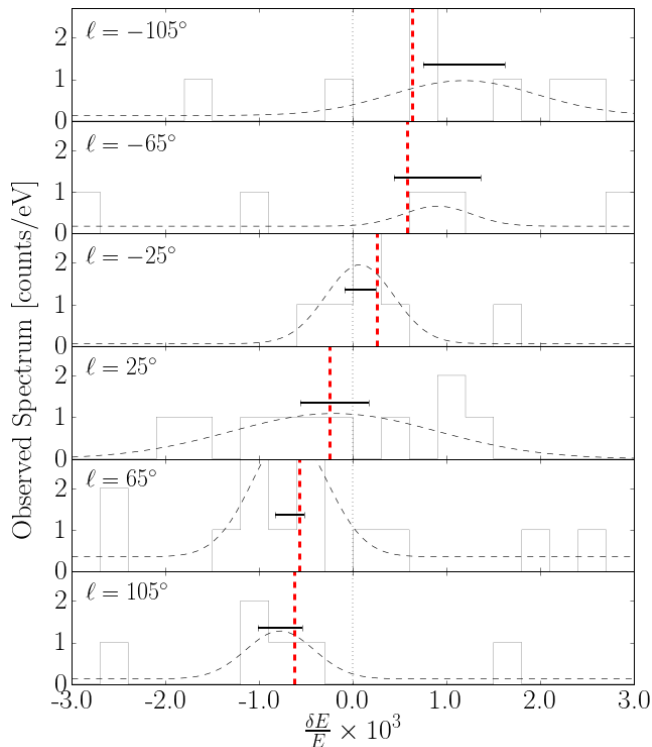
FIG. 3: An example of a synthetic Micro-X observation. The histogram gives the observed photons, though we emphasize that this is only to guide the eye; the likelihood analysis itself is unbinned. The dashed black curves show the model fit, with the horizontal error bars giving the uncertainty in the position of the line centroid. The vertical red dashed lines give the line energy as predicted by the analytic model.

Poisson errors due to N_s and N_b, so that $\sigma_{\rm cent} \sim \left(\frac{\sigma_E^2 + \sigma_{\rm instr}^2}{N_s} \right)^{1/2}$ as expected. We obtain a global significance by summing the significances (the number of $\sigma_{\rm cent}$ by which $\delta E/E = 0$ is excluded) for each pointing in quadrature.

IV Results: Our velocity spectroscopy analysis on N-body data reveals three main insights.

The first is that our analytic model matches the N-body calculation extremely well ($\chi_{\rm red}^2 = 1.8 \times 10^{-3}$). We summarize this result in Figure 6. Furthermore, the simple sinusoid model given by $\Delta E/E = (v_\odot/c) \sin \ell \cos b$ (corresponding to the limit in which the field of view radius goes to zero) also matches the analytic model for Micro-X to within a few percent over the entire range of ℓ ($\chi_{\rm red}^2 = 5.7 \times 10^{-3}$). This line-of-sight integral is thus a sufficient approximation to a large field of view instrument for the given exposure. Note that such small $\chi_{\rm red}^2$ values are due to the large error bars from small N_s. Since $\chi_{\rm red}^2 \propto N_s$, these two models are only differentiable by observations ~ 100 times longer. This suggests that
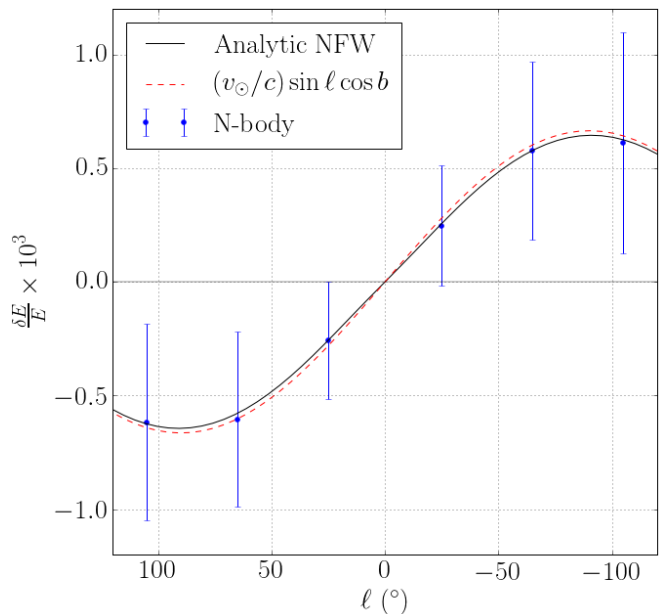

FIG. 6: Velocity spectroscopy on the Milky Way analogue Halo 374. This shows the position of the observed line centroid due to sterile neutrino decay as a function of Galactic longitude ℓ, with latitude $b = 25°$. Here we compare results as computed from the N-body simulation (see Section III B) for the instrumental parameters of Micro-X against our analytic model (Section II) as well as a simple sinusoidal model, showing excellent agreement between the three. Note that the error bars represent σcent, the 1σ uncertainty in the energy of the line centroid, rather than the Doppler-broadened width of the line. For the purposes of this plot and the sky maps (figures 9 and 10), we estimate $\sigma_{\rm cent} = (\sigma_E^2 + \sigma_{\rm instr}^2)^{1/2} C(N_b/N_s) N_s^{-1/2}$, where $C(R) = \sqrt{1 + 4R}$ is a factor given by the optimal Cramer-Rao bound.

for further studies, this sinusoid model is more than sufficient and may be used to quickly explore the parameter space of haloes (e.g. with a Markov chain Monte Carlo) with minimal loss of precision.

The second main result is that combining the observed line energies from the six pointings modeled here ($\ell = \pm 25°, \pm 65°, \pm 105°$ with $b = 25°$) can exclude $\delta E/E = 0$ globally at $\geq 3\sigma$. In 10^5 synthetic observations as described in Section III C, we find that 95% allow a 3σ detection of Doppler shifting. Repeating this experiment for a mission with 10x the exposure, we find that 95% of observations give a $> 8\sigma$ exclusion of $\delta E/E = 0$. See Figure 7 for the full results of this test.

The pointings ℓ centered around $\pm 75°$ exclude $\delta E/E = 0$ with the highest significance, at $\sim 1.5\sigma$. $\ell \sim \pm 75°$ optimizes between two competing effects. The first is the higher J-factor, hence higher photon flux, nearer the Galactic center, giving a smaller uncertainty in the energy of a line detected at small ℓ. The second is that
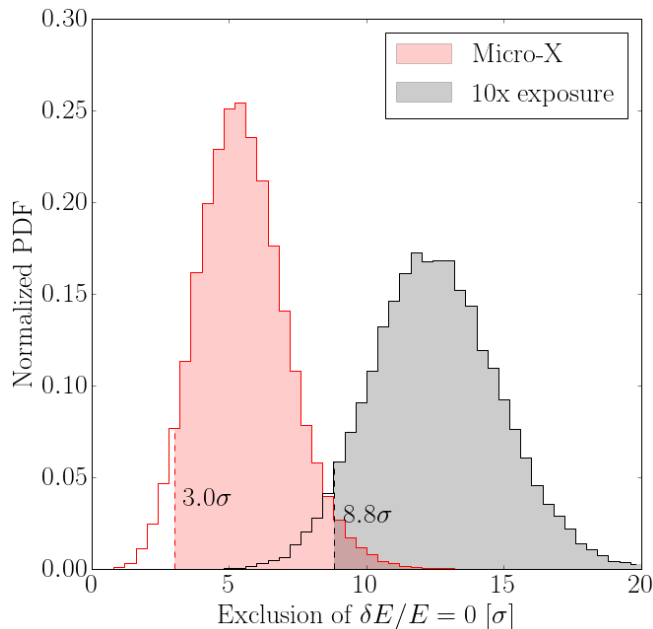
FIG. 7: PDFs of the detection significance for Doppler shifting of the dark matter decay line, given in units of σ. Vertical dashed lines and shaded regions give the 95% confidence interval. We see that for the fiducial Micro-X parameters (red), 95% of observations allow us to exclude $\delta E/E = 0$ globally by 3σ or greater. If we model a hypothetical observing mission with 10x the exposure time (gray), we find that the detection significance increases drastically, giving an 8.8σ detection in 95% of observations. These PDFs were sampled from 10^5 synthetic Micro-X observations. Observations were randomly distributed between all haloes in the simulation suite, with the relative orientation of the Sun to the halo randomized as well.

the mean velocity along the line-of-sight relative to the dark matter increases with ℓ (up to $\ell = 90°$), shifting the observed line further from $\delta E/E = 0$. We illustrate this effect using sky maps in Figure 9. Future observations should focus on these longitudes in order to achieve the best potential detection of this Doppler shift.

Finally, we find that halo triaxiality can bias the significance of a detection to the east or west of the galactic center. When observing above the Galactic plane (in this work, $b = 25°$) any ellipticity of the Galactic halo on the sky can give a higher flux to one side of $\ell = 0°$ than the other. While the mean prediciton for the line centroid matches the analytic model for a spherical halo quite well, observing to one side of the GC allows one to exclude $\delta E/E = 0$ with higher significance due to better photon counting statistics. This is illustrated in Figure 10. We also find that the effect of subhaloes on our observations are small, with only $\sim 1\%$ of pointings seeing over 10% of the flux contributed by a single subhalo (Figure 8). This supports intuition in that the closest approach of

subhaloes in our simulations is ~ 40 kpc, so the smooth component of the main halo is expected to dominate the signal.
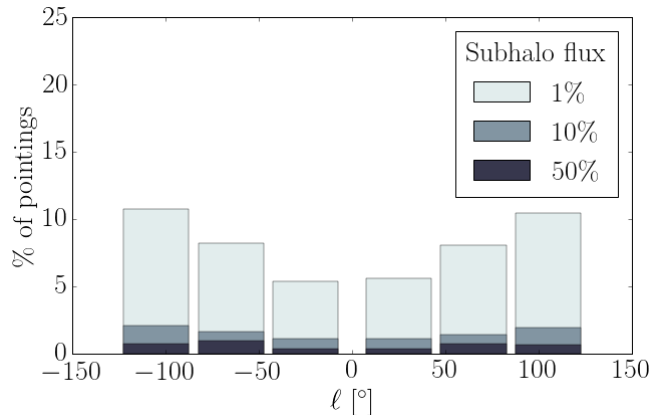

FIG. 8: The contribution of subhaloes to the total observed DM decay flux. The bars give the fraction of all Micro-X pointings containing a subhalo that contributes more than some fraction of the total flux. I.e., we find that at $\ell = 105°$, about 10% of pointings contain a subhalo bright enough to contribute over 1% of the total flux for that pointing. The number of pointings dominated by (10% or 50% of total flux) a single subhalo is low, at the $\sim 1\%$ level.

V Conclusions:

Very often in the past, anomalous astrophysical signals have been interpreted as the signature of dark matter. However, none of these extraordinary claims survived the scrutiny of extraordinary evidence. All of these false alarms raises an important question: can we design a new test to confirm the dark matter origin of an anomalous astrophysical signal? The answer is yes, and Ref. [1] showed that telescopes with $\mathcal{O}(0.1\%)$ energy resolution can utilize the Doppler effect of a sharp signal arising from dark matter interactions to perform dark matter velocity spectroscopy.

We look into this issue in detail in this work using synthetic observations generated from a suite of N-body simulations [22].

We find that a Micro-X-like observation (total exposure $\sim 10^3$ cm^2 str s between all pointings) can reliably confirm the Doppler shifting effect on a sterile netrino decay line at 3σ or better. The best design for such an observation consists of pointings centered around galactic longitude $\ell \sim \pm 75°$ and latitude $b = 25°$, as this gives the optimal balance between the magnitude of the Doppler shift and the signal to noise ratio.

We find that although we give the fully analytic treatment for a large (20° radius) field of view instrument, the simple sinusoidal model for the Doppler shifting signature $\Delta E/E = (v_\odot/c)\sin\ell\cos b$ is more than sufficiently accurate for the photon statistics considered here. Only for a 100x longer observation will the small and large field of

0.005 photons cm^{-2} str^{-1} s^{-1} 0.4

(a) Flux.

-1 $\frac{\delta E}{E} \times 10^3$ 1
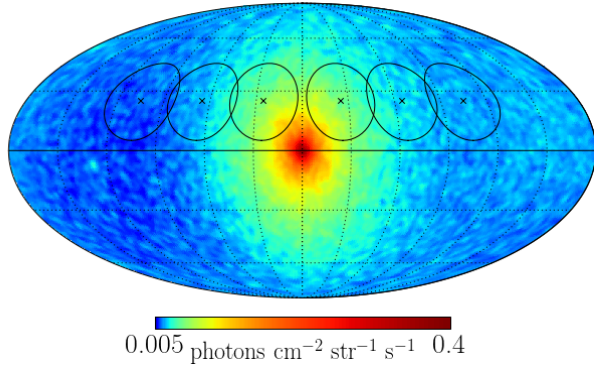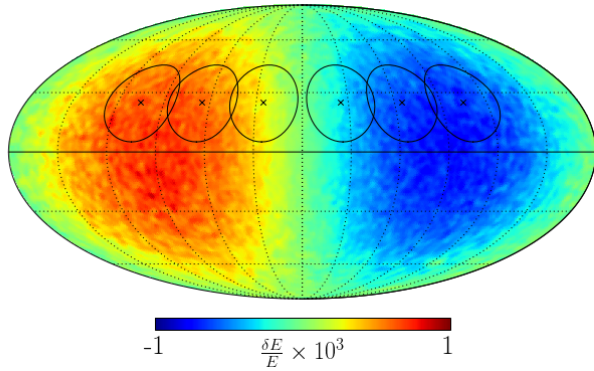
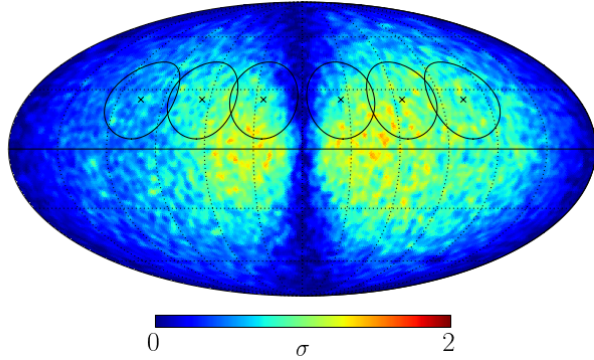(b) Doppler-shifted line centroid.

0   σ 2

(c) Exclusion of the line centroid from $\delta E/E = 0$.

FIG. 9: Sky maps illustrating the principle of velocity spectroscopy. Top: The flux map. Middle: The dipole pattern in the line energy induced by our motion relative to the Milky Way halo. Bottom: The signicance of the detection of Doppler shifting of a dark matter decay line, indicating the number of σ by which $\delta E/E = 0$ can be excluded for a Micro-X observation. Black circles indicate the FOV of Micro-X on the sky for the six pointings used in Figure 6.

view models be differentiable.

We also note that while a spherical NFW model for a dark matter halo is quite accurate, halo triaxiality does have an effect on the significance of the detection. The

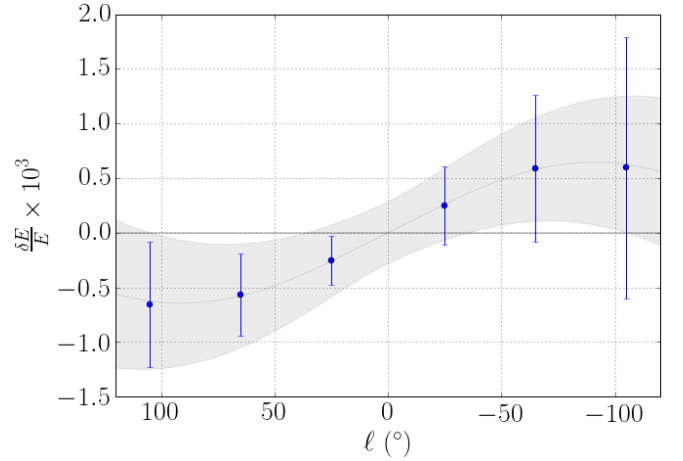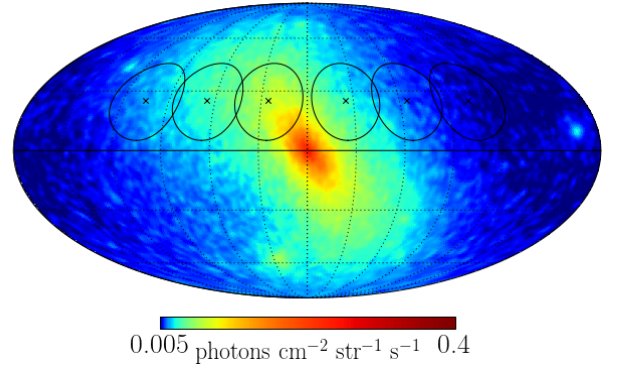0.005 photons cm^{-2} str^{-1} s^{-1} 0.4

FIG. 10: Asymmetry of the Milky Way halo (here, Halo 800 with $b/a =$ and $c/a =$) could skew the significance of the observed signal to the east or west. Each field of view (black circles in the sky map) corresponds to a data point in the lower plot. The gray shaded region indicates the 1σ uncertainties for the analytic model derived from a spherical NFW profile fit to this halo.

effects of subhaloes are also considered but found to be small.

We have cause for optimism for future experiments. While Micro-X is a good model for a first observation of dark matter velocity spectroscopy in the Milky Way, future high resolution X-ray spectrographs are sure to provide the modest increase in photon counts needed for a high-significance detection. Increasing the duration of the model Micro-X exposure by a factor of 10 gives at least an 8σ detection of the Doppler effect on dark matter decay photons.

We emphasize that although we focus on the 3.5 keV line here, the theoretical and observational concepts laid out here are applicable to photons arising from *any* dark matter decay process.

[1] E. G. Speckhard, K. C. Y. Ng, J. F. Beacom, and R. Laha, Physical Review Letters 116, 031301 (2016), arXiv:1507.04744.

[2] G. Jungman, M. Kamionkowski, and K. Griest, Phys. Rept. 267, 195 (1996), arXiv:hep-ph/9506380 [hep-ph].

[3] G. Bertone, D. Hooper, and J. Silk, Phys. Rept. 405, 279 (2005), arXiv:hep-ph/0404175 [hep-ph].

[4] L. E. Strigari, Phys. Rept. 531, 1 (2013), arXiv:1211.7090 [astro-ph.CO].

[5] G. Bertone and D. Hooper, Submitted to: Rev. Mod. Phys.(2016), arXiv:1605.04909 [astro-ph.CO].

[6] M. Klasen, M. Pohl, and G. Sigl, Prog. Part. Nucl. Phys. 85, 1 (2015), arXiv:1507.03800 [hep-ph].

[7] M. Loewenstein and A. Kusenko, Astrophys. J. 714, 652 (2010), arXiv:0912.0552 [astro-ph.HE].

[8] D. A. Prokhorov and J. Silk, Astrophys. J. 725, L131 (2010), arXiv:1001.0215 [astro-ph.HE].

[9] C. Weniger, JCAP 1208, 007 (2012), arXiv:1204.2797 [hep-ph].

[10] K. N. Abazajian, N. Canac, S. Horiuchi, M. Kaplinghat, and A. Kwa, JCAP 1507, 013 (2015), arXiv:1410.6168 [astro-ph.HE].

[11] S. K. Lee, M. Lisanti, B. R. Safdi, T. R. Slatyer, and W. Xue, Phys. Rev. Lett. 116, 051103 (2016), arXiv:1506.05124 [astro-ph.HE].

[12] R. Bartels, S. Krishnamurthy, and C. Weniger, Phys. Rev. Lett. 116, 051102 (2016), arXiv:1506.05104 [astro-ph.HE].

[13] E. Bulbul, M. Markevitch, A. Foster, R. K. Smith, M. Loewenstein, and S. W. Randall, Astrophys. J. 789, 13 (2014), arXiv:1402.2301 [astro-ph.CO].

[14] A. Boyarsky, O. Ruchayskiy, D. Iakubovskyi, and J. Franse, Phys. Rev. Lett. 113, 251301 (2014), arXiv:1402.4119 [astro-ph.CO].

[15] O. Urban, N. Werner, S. W. Allen, A. Simionescu, J. S. Kaastra, and L. E. Strigari, Mon. Not. Roy. Astron. Soc. 451, 2447 (2015), arXiv:1411.0050 [astro-ph.CO].

[16] R. M. O'Leary, M. D. Kistler, M. Kerr, and J. Dexter(2015), arXiv:1504.02477 [astro-ph.HE].

[17] T. D. Brandt and B. Kocsis, Astrophys. J. 812, 15 (2015), arXiv:1507.05616 [astro-ph.HE].

[18] R. M. O'Leary, M. D. Kistler, M. Kerr, and J. Dexter(2016), arXiv:1601.05797 [astro-ph.HE].

[19] L. Gu, J. Kaastra, A. J. J. Raassen, P. D. Mullen, R. S. Cumbee, D. Lyons, and P. C. Stancil, Astron. Astrophys. 584, L11 (2015), arXiv:1511.06557 [astro-ph.HE].

[20] K. J. H. Phillips, B. Sylwester, and J. Sylwester, Astrophys. J. 809, 50 (2015).

[21] C. Shah, S. Dobrodey, S. Bernitt, R. Steinbrugge, J. R. C. Lopez-Urrutia, L. Gu, and J. Kaastra(2016), arXiv:1608.04751 [astro-ph.HE].

[22] Y.-Y. Mao, M. Williamson, and R. H. Wechsler, Astrophys. J. 810, 21 (2015), arXiv:1503.02637.

[23] D. Iakubovskyi(2015), arXiv:1510.00358 [astro-ph.HE].

[24] T. E. Jeltema and S. Profumo, Mon. Not. Roy. Astron. Soc. 458, 3592 (2016), arXiv:1512.01239 [astro-ph.HE].

[25] O. Ruchayskiy, A. Boyarsky, D. Iakubovskyi, E. Bulbul, D. Eckert, J. Franse, D. Malyshev, M. Markevitch, and A. Neronov, Mon. Not. Roy. Astron. Soc. 460, 1390 (2016), arXiv:1512.07217 [astro-ph.HE].

[26] E. Bulbul, M. Markevitch, A. Foster, E. Miller, M. Bautz, M. Loewenstein, S. W. Randall, and R. K. Smith(2016), arXiv:1605.02034 [astro-ph.HE].

[27] F. A. Aharonian et al. (Hitomi)(2016), arXiv:1607.07420 [astro-ph.HE].

[28] F. Hofmann, J. S. Sanders, K. Nandra, N. Clerc, and M. Gaspari, Astron. Astrophys. 592, A112 (2016), arXiv:1606.04091 [astro-ph.CO].

[29] C. A. Arguelles, V. Brdar, and J. Kopp(2016), arXiv:1605.00654 [hep-ph].

[30] J. P. Conlon, F. Day, N. Jennings, S. Krippendorf, and M. Rummel(2016), arXiv:1608.01684 [astro-ph.HE].

[31] A. Neronov, D. Malyshev, and D. Eckert(2016), arXiv:1607.07328 [astro-ph.HE].

[32] K. Perez, K. C. Y. Ng, J. F. Beacom, C. Hersh, S. Horiuchi, and R. Krivonos(2016), arXiv:1609.00667 [astro-ph.HE].

[33] E. Figueroa-Feliciano et al. (XQC), Astrophys. J. 814, 82 (2015), arXiv:1506.05519 [astro-ph.CO].

[34] T. M. Dame, D. Hartmann, and P. Thaddeus, Astrophys. J. 547, 792 (2001), arXiv:astro-ph/0009217 [astro-ph].

[35] R. Diehl et al., Nature 439, 45 (2006), arXiv:astro-ph/0601015 [astro-ph].

[36] P. M. W. Kalberla and L. Dedes, Astron. Astrophys. 487, 951 (2008), arXiv:0804.4831 [astro-ph].

[37] K. Kretschmer, R. Diehl, M. Krause, A. Burkert, K. Fierlinger, O. Gerhard, J. Greiner, and W. Wang, Astron. Astrophys. 559, A99 (2013), arXiv:1309.4980 [astro-ph.HE].

[38] D. Attie et al., Astronomy and Astrophysics 411, L71 (2003), arXiv:astro-ph/0308504.

[39] D. Barret et al.(2016), doi:\bibinfo{doi}{10.1117/12.2232432}, arXiv:1608.08105 [astro-ph.IM].

[40] N. Bozorgnia, F. Calore, M. Schaller, M. Lovell, G. Bertone, C. S. Frenk, R. A. Crain, J. F. Navarro, J. Schaye, and T. Theuns, JCAP 1605, 024 (2016), arXiv:1601.04707 [astro-ph.CO].

[41] J. D. Sloane, M. R. Buckley, A. M. Brooks, and F. Governato(2016), arXiv:1601.05402 [astro-ph.GA].

[42] C. Kelso, C. Savage, M. Valluri, K. Freese, G. S. Stinson, and J. Bailin(2016), arXiv:1601.04725 [astro-ph.GA].

[43] V. Springel, M.N.R.A.S. 364, 1105 (2005), arXiv:astro-ph/0505010.

[44] T. Venumadhav, F.-Y. Cyr-Racine, K. N. Abazajian, and C. M. Hirata, Phys. Rev. D 94, 043515 (Aug. 2016), arXiv:1507.06655.

[45] M. R. Lovell, G. Bertone, A. Boyarsky, A. Jenkins, and O. Ruchayskiy, Mon. Not. Roy. Astron. Soc. 451, 1573 (2015), arXiv:1411.0311 [astro-ph.CO].

[46] V. P. Debattista, B. Moore, T. R. Quinn, S. Kazantzidis, R. Maas, L. Mayer, J. Read, and J. Stadel, Astrophys. J. 681, 1076 (2008), arXiv:0707.0737 [astro-ph].

[47] S. E. Bryan, S. T. Kay, A. R. Duffy, J. Schaye, C. D. Vecchia, and C. M. Booth, Mon. Not. Roy. Astron. Soc. 429, 3316 (2013), arXiv:1207.4555 [astro-ph.CO].

[48] N. Bernal, J. E. Forero-Romero, R. Garani, and S. Palomares-Ruiz, JCAP 1409, 004 (2014), arXiv:1405.6240 [astro-ph.CO].

[49] N. Bernal, L. Necib, and T. R. Slatyer(2016), arXiv:1606.00433 [astro-ph.CO].

[50] Y.-Y. Mao, L. E. Strigari, R. H. Wechsler, H.-Y. Wu, and O. Hahn, Astrophys. J. **764**, 35 (2013), arXiv:1210.2721 [astro-ph.CO].

[51] D. McCammon *et al.*, Astrophys. J. **576**, 188 (2002), arXiv:astro-ph/0205012 [astro-ph].

[52] A. Boyarsky, J. W. den Herder, A. Neronov, and O. Ruchayskiy, Astropart. Phys. **28**, 303 (2007), arXiv:astro-ph/0612219 [astro-ph].

[53] S. G. Crowder *et al.*, Astrophys. J. **758**, 143 (2012), arXiv:1209.1657 [astro-ph.HE].

[54] M. Ajello *et al.*, Astrophys. J. **689**, 666 (2008), arXiv:0808.3377 [astro-ph].

[55] R. C. Hickox and M. Markevitch, Astrophys. J. **645**, 95 (2006), arXiv:astro-ph/0512542 [astro-ph].

[56] R. Barlow, Nuclear Instruments and Methods in Physics Research Section A: Accelerators, Spectrometers, Detectors and Associated Equipment **297**, 496 (1990), ISSN 0168-9002, http://www.sciencedirect.com/science/article/pii/0168900290913348.